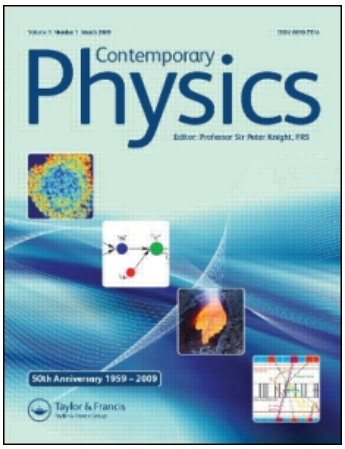

Contemporary Physics
Publication details, including instructions for authors and subscription information:
http://www.informaworld.com/smpp/title~content=t713394025

An introduction to the physics of the bacterial flagellar motor: a nanoscale rotary electric motor

Matthew A. B. Baker [a]; Richard M. Berry [a]
[a] Clarendon Laboratory, Department of Physics, University of Oxford, Oxford, UK

Online Publication Date: 01 November 2009

To cite this Article Baker, Matthew A. B. and Berry, Richard M.(2009)'An introduction to the physics of the bacterial flagellar motor: a nanoscale rotary electric motor',Contemporary Physics,50:6,617 — 632
To link to this Article: DOI: 10.1080/00107510903090553
URL: http://dx.doi.org/10.1080/00107510903090553

Contemporary Physics
Vol. 50, No. 6, November–December 2009, 617–632

Taylor & Francis
Taylor & Francis Group

An introduction to the physics of the bacterial flagellar motor: a nanoscale rotary electric motor

Matthew A.B. Baker and Richard M. Berry*

Clarendon Laboratory, Department of Physics, University of Oxford, Parks Road, Oxford OX1 3PU, UK

(*Received 23 April 2009; final version received 3 June 2009*)

Biological molecular motors show us how directed motion can be generated by nanometre-scale devices that work at the energy scale of the thermal bath. Direct and indirect observations of functioning single molecule motors allow us to see fundamental processes of statistical physics unfolding in microscopic detail at room temperature, something that was unimaginable only a few decades ago. In this review, we introduce molecular motors and the physics relevant to their mechanisms before focusing on our recent experiments on the bacterial flagellar motor, the rotary device responsible for bacterial locomotion.

Keywords: biological molecular motors; nanometre-scale devices

1. Introduction

Directed movement is a signature of life, and essential to movement is the ability to generate force. In biological systems it is motor proteins that generate force. Motor proteins are large molecules which use chemical energy to do work and are responsible for motility across all levels: for transport within a cell, for the motion of an individual cell in its surroundings, and for movement in multi-cellular aggregates, such as muscles. The bacterial flagellar motor is an example of a meso-scale cluster of proteins, including several motor proteins, that work together to provide the locomotive force for bacteria.

1.1. Motor proteins

Proteins are the main functional elements in molecular biology, but may be less familiar to physicists than biologists. They are large fluctuating molecules that perform a specific function based upon their structure, which depends in turn on the way they are *folded* [1]. Little is known about the details of how folding is controlled or directed and it is one of the central questions of biology. One thing that is clear, however, is that correctly folded proteins are only just stable. This marginal stability allows proteins to make transitions between several different meta-stable structures or *conformations*. These *conformational changes* underlie the mechanisms of most proteins, of which molecular motors are a particularly clear example.

Motor proteins couple conformational changes to chemical reactions that release free energy, using these *mechanochemical transitions* to generate force and make things move. At the molecular level linear-motor proteins such as kinesins, myosins and dyneins are responsible for hauling components directionally inside a cell along fixed tracks, carrying cargos attached to their tails. When many motor proteins work in concert, macroscale motion can be generated. For example, the linear motor protein, myosin, is responsible for exerting a small force on an actin filament [2]. Myosin is the driving force behind muscle contraction. When you lift your arms, billions of myosin molecules are pulling arrays of parallel actin filaments together, contracting your biceps [3,4].

At the cellular level, there are many cells that can move around their environment. One example is the sperm cell, which generates motion by a coordinated oscillation of linear dynein motors that generates wave propagation in the tail [5]. Another example is phagocytes, part of the immune system, which move by using linear motors to distort their structure and 'crawl' along surfaces [6]. There are also examples of multicellular motion and cooperation in amoebic moulds such as dictyostelium. Dictyostelium cells move as multicellular aggregates, and when they receive a chemical signal can form 'fruiting bodies' that move en masse to form mushroom-like structures. This is an early demonstration of cooperativity where single cell organisms can coordinate their motion to benefit the aggregate at the expense of some individual cells [7]. Figure 1 shows these different examples of motor motility.

1.2. The bacterial flagellar motor

The bacterial flagellar motor (BFM) is a self-assembled protein complex ~ 50 nm in diameter embedded in the bacterial cell envelope, which is capable of rotating at speeds up to 100,000 rpm, five times as fast as a

*Corresponding author. Email: r.berry1@physics.ox.ac.uk

ISSN 0010-7514 print/ISSN 1366-5812 online

DOI: 10.1080/00107510903090553
http://www.informaworld.com

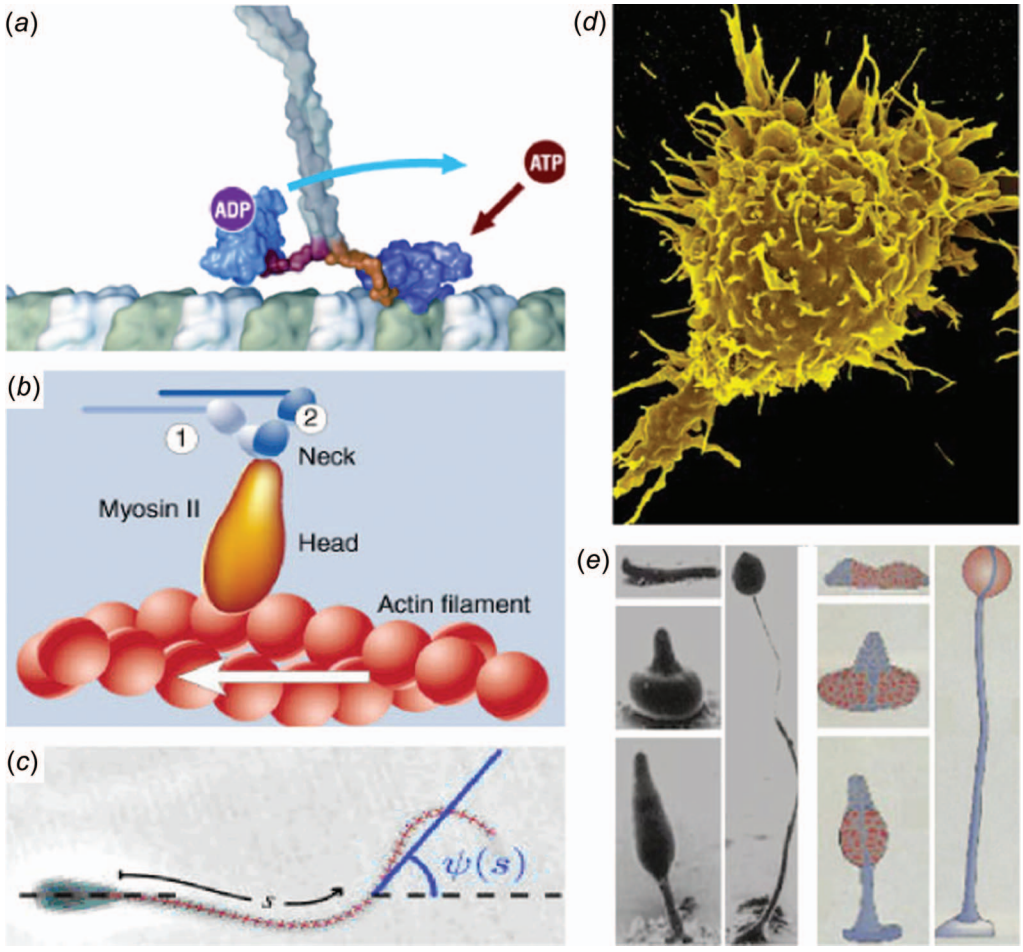

Figure 1. Different types of motility. (*a*) Kinesin moving along a microtubule. The dimer is entwined and the two heads walk along a microtubule in a hand-over-hand mechanism. Shown here is one state in the chemical cycle, where ATP is bound at the head attached to the track and ADP is released from the trailing head [8]. Reprinted with permission from T.D. Pollard and W.C. Earnshaw, *Cell Biology*, W.B. Saunders, Kidlington, 2002. Copyright (2002) by Elsevier. (*b*) Myosin II, one of the molecular motors responsible for muscle contraction, pulls an actin filament. In muscles, tail sections of Myosin II bundle to form the *thick filament*, and actin bundles to form the *thin filament*. The sliding of thick against thin filaments, driven by Myosin II, is what causes muscle contraction [9]. Reprinted with permission from Nature, 408 (2000), pp. 764–766. Copyright (2000) by Nature Publishing Group. (*c*) Flagellar beating in sperm due to coordinated oscillation of dyneins acting on microtubules in the tail of sperm [5]. Reprinted with permission from HFSP J., 1 (2007), pp. 192–208. Copyright (2001) by HFSP Publishing. (*d*) A SEM image of a phagocyte [10]. Reprinted with permission from Nat. Rev. Moll. Cell Biol., 4 (2003), pp. 385–396. Copyright (2003) by Nature Publishing Group. (*e*) Left: SEM images of dictyostelium aggregates forming fruiting bodies and raising off a surface. Right: blue shows prestalk cells and red prespore cells. To form a fruiting body these cells sort themselves and move into position signalling to each other using chemotaxis [7]. Reprinted with permission from Microbiology, 146 (2000), pp. 1505–1512. Copyright (2000) by the Society for General Microbiology.

modern Formula 1 engine [11]. BFMs from several species have been studied, and all are broadly similar. In this article we will refer to the motors of *Escherichia coli* (*E. coli*) and *Salmonella typhimurium* (*S. typhimurium*) unless otherwise stated, as these are the most studied and best understood examples. The motor is powered by ions crossing the cell membrane, driven by electrical and chemical potential differences, and uses this energy to rotate either clockwise or counterclockwise, switching in response to environmental signals. Motor rotation is coupled to helical flagellar filaments through the *hook*, a helical protein polymer which acts as a universal joint. When filaments are rotated counterclockwise (CCW, looking down the filament towards the cell) they form bundles which propel the swimming cell. When they are rotated in the opposite direction, one or more filaments splay from the bundle initiating a 'tumble', which is a random re-orientation of the cell. Tumbles are suppressed when a cell detects that the concentration of attractant molecules in its environment is increasing, prolonging episodes when the cell is swimming to where things are better. In this way cells can execute a biased random walk that moves

them towards regions of increased nutrient concentration, a process known as *chemotaxis*. Much has been learned about chemotaxis [12–14] but we will not discuss it here.

The BFM contains ~13 different proteins. Aggregates of these proteins make up larger structures, such as rods and rings, which are assembled in a specific order using guided self-assembly. The *basal body* of the motor assembles first. This consists of four rings and a rod which acts as a driveshaft to the filament, and it is the core of the motor. The basal body is assembled across the cell wall, with one of its rings, the MS ring, assembled first as the platform on which the rest of the motor is mounted. The C ring of the basal body, made from FliG, FliM, and FliN proteins, contains a ring of ~26 FliG molecules which are believed to be the site of torque-generating rotor/stator interactions. Each motor contains several independent stators, membrane–protein complexes each containing the proteins MotA and MotB. Stators assemble after the basal body and can bind into and dissociate away from the motor while the motor is operating. This results in speed jumps as the stators come and go, and there can be up to at least 11 stators in a motor at any time [15]. We confirmed this dynamic picture of a molecular machine that is constantly being re-configured 'on the fly' by single-molecule fluorescence microscopy of motors with fluorescently labelled stator proteins [16]. The average lifetime of a given stator in the motor was found to be less than one minute. This surprising result has posed the question: are all protein complexes similarly dynamic, or are the BFM stators unusual in this respect? The remaining proteins that constitute the hook and the filament are exported via a Type III pathway, which signifies that they are transported to the tip using diffusion, through the hollow interior of a well-defined structure. In the BFM they diffuse through a channel that runs inside the hook and filament. The structure of the BFM is shown in Figure 2; for a review of structure and assembly see [17].

Bacteria propel themselves effectively at low Reynold's number, R, a measure of the relative magnitude

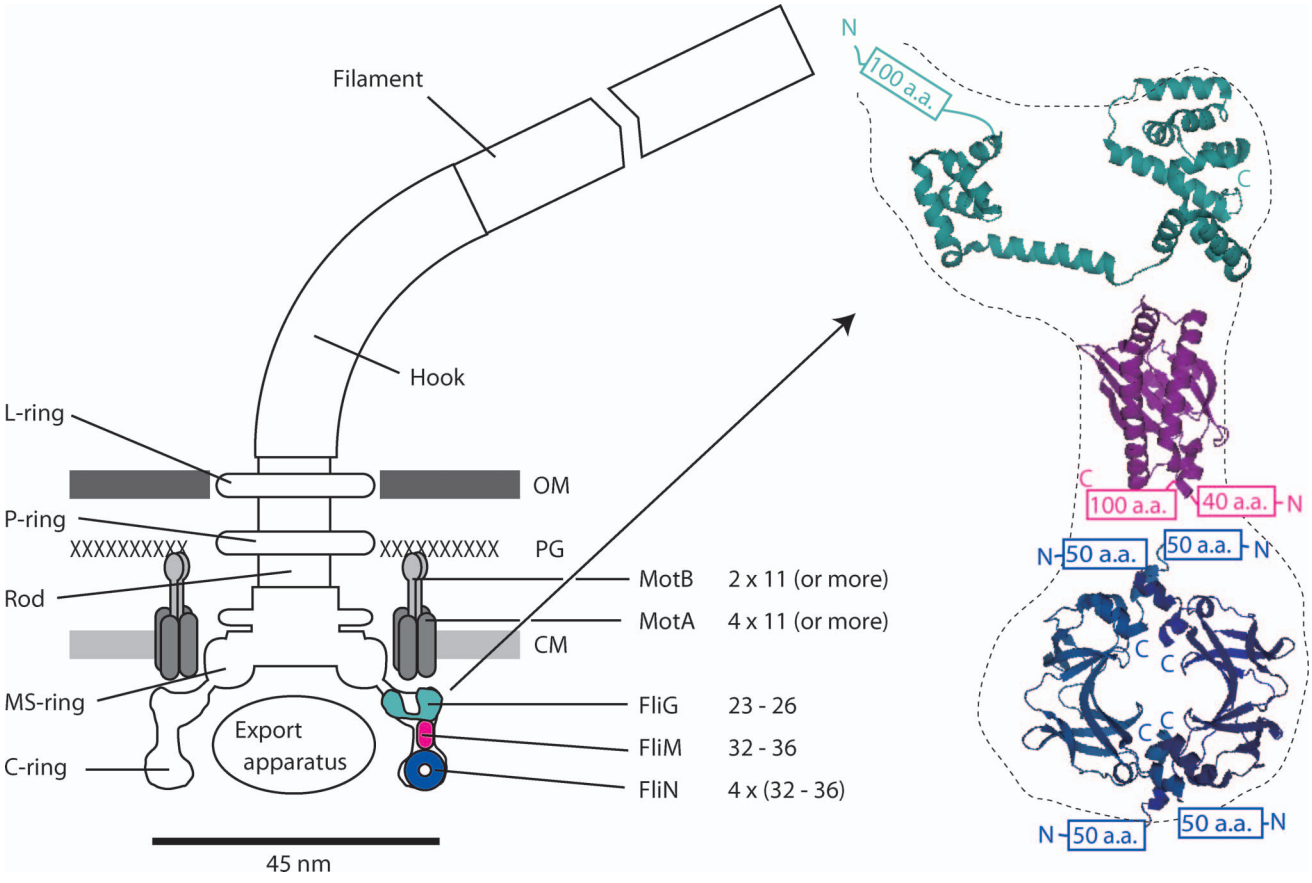

Figure 2. Left: schematic side-view of the BFM, with the proposed location and copy number of proteins involved in torque generation. The basal body consisting of the C-ring, MS-ring, rod, P-ring and L-ring, assembles first, followed by the hook and filament proteins. The stators are dynamic and each has the stoichiometry $MotA_2$ $MotB_4$. Right: detail of the proposed location and orientation of the three C-ring proteins. X-ray crystal structures of truncated rotor proteins, FliG (Cyan), FliM (Magenta) and FliN (Blue), are shown docked into the C-ring structure. N- and C-termini and unresolved amino acids are indicated. Figure reproduced from Sowa and Berry [11]. Reprinted with permission from Q. Rev. Biophys., 41 (2008), pp. 103–132. Copyright (2008) by Cambridge University Press.

of viscous and inertial forces, which is $\sim 10^{-4}$ for a swimming bacterium. They do this by rotating the helical filament in a non-reciprocal cyclical movement. Non-reciprocal motion is necessary for propulsion at low R, where the equations of fluid mechanics become time-reversible and thus reciprocal motion generates no propulsion [18]. Transport in this regime is measured against diffusion. In order for bacteria to benefit from swimming they must 'outrun' diffusion to a region of higher nutrient concentration. Bacteria can swim in a straight line for only a few seconds, before Brownian motion re-orients them randomly. A typical nutrient molecule has a diffusion coefficient of $\sim 400\ \mu m^2\ s^{-1}$ which means that diffusion will carry it $\sim 70\ \mu m$ in 2 s. Typical swimming speeds are in the range 40–60 $\mu m\ s^{-1}$ so swimming driven by the flagellar motor does indeed help, but only just.

2. The physics of molecular motors

2.1. Biological free energy

Molecular motors, by their nature, are directional and do work against a load. These directional processes occur in an environment dominated by fluctuation, and the small parts that make up these motors operate at energies only marginally higher than the thermal bath. This is the central difference between macroscopic and molecular motors and these fluctuations are an essential component of the motor mechanism. Macroscopic ideas of atomic-scale components working as levers, cogs, wheels and pistons are useful to some extent, but do not convey the fact that these interactions are occurring in a fluctuating viscous environment, driven by energetic and entropic considerations. Motion occurs by biasing this fluctuation in such a way that work is achieved.

This work is coupled to a *free-energy* source, usually the hydrolysis of a molecule such as ATP, the so-called energy currency of life. Kinesin and myosin are both examples of ATP-driven molecular motors which use the free energy released by hydrolysing ATP to power their mechanochemical transitions. Most biological processes occur at constant temperature and pressure, so the relevant free energy which determines whether a process will proceed or not is the Gibbs free energy. The change in Gibbs free energy, ΔG, is defined as the enthalpic change minus the temperature-weighted entropic change:

$$\Delta G = \Delta H - T\Delta S,$$

and must be negative (transient fluctuations are not subject to this law, as described by fluctuation theorems [19], but the mechanochemical cycles of molecular motors are). Molecular motors perform work by using the free energy produced by an associated chemical reaction to compensate for free energy consumed when mechanical work is done.

The BFM is unusual among molecular motors in that it is powered by an *electrochemical* rather than a purely chemical process, namely the transit of monovalent cations across the cell membrane. The free energy per unit charge crossing the membrane is called the ion motive force (IMF), and has units of volts. The IMF arises from active metabolic transport of ions (usually protons, H^+) across energised biological membranes, and is a key intermediate in bioenergetics [1]. The IMF has electrical and chemical components, and is defined by:

$$\mathrm{IMF} = V_m + \frac{kT}{q}\ln\left(\frac{C_i}{C_0}\right),$$

where V_m is the voltage difference across the membrane (normally negative inside), k is Boltzmann's constant, T is the absolute temperature, q is the ionic charge, and C_i and C_o are the ion concentrations inside and outside the cell, respectively. The two parts of the IMF can be considered separately: as an enthalpic component, V_m, and an entropic component, $\Delta\mu/q = (kT/q)\ln(C_i/C_o)$. The enthalpic component is the electrostatic energy gain that arises when an ion moves from outside the cell to inside the cell across the voltage drop located at the membrane. The entropic component is the chemical potential difference per unit charge due to the concentration difference across the membrane.

It is worth mentioning here that nearly all living systems function only in aqueous solution at temperatures near room temperature, and that the free-energy changes associated with their function are comparable to the thermal energy, kT. Thus, it is convenient to introduce an appropriate energy scale based on units of kT_0, where T_0 is room temperature. We will use $kT_0 = 4 \times 10^{-21}$ J. In terms of mechanical work, this can also be written as 4 pN nm. Under typical biological conditions, the hydrolysis of one molecule of ATP produces $\sim 20kT_0$ of free energy, and a single ion transit $\sim 6kT_0$.

2.2. Physical descriptions of molecular motors

To understand the relationship between the chemical driving force and the mechanical force or torque that it generates, we need to build a framework where we can describe the mechanochemical transitions that couple chemical reactions to the conformational changes that make the motor move. Molecular motors are large molecular complexes with many interacting parts. Ideally our framework should accurately describe our system, but not be prohibitively complex. The most detailed method of modelling a macromolecular

system is to use *Molecular Dynamics* (MD) to simulate the trajectories of every atom in the system. If we have N atoms, the full MD description of the system includes $6N$ degrees of freedom: three for velocity and three for position of each atom in the system and surrounding solvent water molecules. At each time step and for each atom, Newton's equations of motion are combined with empirical pair-wise force-fields and used to calculate the net force on each atom. For the next time step all the atoms are moved into their predicted new positions, and so on. Due to the computational intensity of MD, only picosecond to nanosecond timescales can be simulated for large protein complexes such as molecular motors. This compares to millisecond and slower timescales for the working cycles of a typical molecular motor. Some progress is being made in *coarse-grained* MD, where several atoms are grouped together into pseudo-atoms, each a separate software object. However, the force-fields for these pseudo-atoms are not so well tested as those for all-atom MD, and the computational gains are not yet enough to allow simulation of full cycles of molecular motors.

At the opposite end of the scale from MD, the least detailed description of a macromolecular system is entirely kinetic. Kinetic models define discrete states of the system that are separated by free-energy barriers, and model transitions between these states as instantaneous thermally activated jumps over the energy barriers, following the classical Eyring or Kramers theories [20,21]. Figure 3 shows a simple four state kinetic model, with the free-energy barrier shown for the transition between state A and state B. In the case of molecular motors, coupling between the chemical driving force and mechanical output is ensured by assuming that each state corresponds to a particular mechanical as well as chemical configuration of the system.

Kinetic models can be useful in analysing simple features of molecular motors, as we describe in Section 3.3 below. However, they do not really explore the physical mechanism of coupling, which is lost in the *a priori* assumption of coupled mechanical and chemical properties of each state. The most useful level of description of molecular motors dates back to the 1950s [22,23] and consists of solving *Langevin* or *reaction-diffusion* equations. This is known as *Brownian Dynamics*. In the all-atom simulations of MD, most degrees of freedom correspond to thermal fluctuations which are not significant when modelling the mechanical action of the motor. The essential motion of a molecular motor may be described more simply by a stochastic differential equation (a *Langevin equation*) in which thermal fluctuations are modelled by an uncorrelated random force representing the effect of

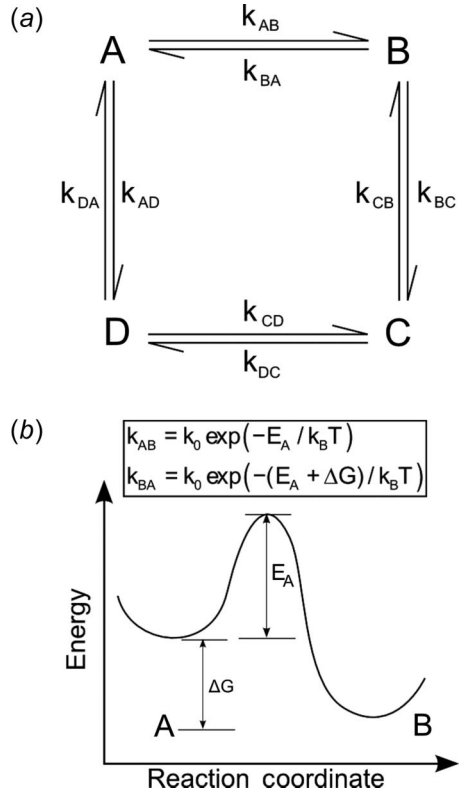

Figure 3. A four-state kinetic model where distinct states of the system are assumed to be connected by instantaneous transits. Transitions from one state to another can be characterised by a *reaction coordinate*, an abstraction of the multiple pathways that the system can follow between any two states. In each case an energy barrier must be overcome to initiate the change in state, and the change from one state to another is modelled as a Poisson process with a constant probability k_{ij} of occurring per unit time. The constants k_{ij} are called *rate constants*, and the principle of Detailed Balance requires that $k_{AB}/k_{BA} = \exp(-\Delta G/kT)$ for any transition A $\leftrightarrow$ B. The equations shown in the figure obey this condition and are usually used as a starting point for describing rate constants in a kinetic model of a molecular motor.

the solvent on the motor. Brownian Dynamics begins by considering only those degrees of freedom which are necessary to describe the chemical and mechanical processes of the motor. We define an *energy landscape*, a multi-dimensional state space in which each point represents one configuration of the motor and an associated free energy, the potential of mean force. The landscape contains within it macrostates that are collections of configurations which share important properties, for example a major conformational property such as the relative position of a pair of rotor and stator proteins, or a major chemical property such as whether and where an ATP molecule is bound. For a simple ATP-driven motor such as a single kinesin or myosin head, the chemical dimension or variable would represent the binding and subsequent

hydrolysis of ATP, followed by release of the products ADP and phosphate. For the BFM, it would represent ion transit across the membrane. It is also possible to have more than one chemical variable, for example the rotary molecular motor F_1-ATPase has three, one for each of the three ATP binding sites located symmetrically around the rotor [24,25].

The energy landscape of a molecular motor will have local maxima and minima and pathways between minima that couple chemical energy to mechanical work. The landscape is typically periodic in both reaction and position coordinates, which reflects the cyclic nature of molecular motors. Figure 4 illustrates a hypothetical landscape with one chemical and one mechanical variable. The chemical energy decreases from left to right, indicating the direction of the driving reaction. The mechanical energy increases from bottom to top, indicating work done against a conservative force or torque. Diagonal valleys in the landscape lead to coupling between chemical and mechanical variables, the fundamental function of the motor. Mechanochemical states correspond to wells in the landscape, and are indicated by A, B, C in Figure 4(*a*).

After the reduction in the number of degrees of freedom of the system, the second major ingredient of Brownian Dynamics is separation of timescales between chemical and mechanical processes. Ion transits and chemical reactions involve small, local motions, such as the movement of a single ion or the breaking of a single covalent bond in ATP hydrolysis. These chemical processes occur on timescales of microseconds or faster. By contrast, mechanical changes such as large-scale conformational changes in a protein or relative motions of different proteins or groups of proteins (for example rotation of the BFM rotor relative to the stators) are much slower, with millisecond timescales. Brownian Dynamics takes advantage of this timescale separation by treating the slow, mechanical variables as continuous, and discretising the chemical variables into a set of kinetic states. Each chemical state is represented by an energy profile (versus mechanical variables), which can be thought of as a section of the energy landscape at a fixed value of the chemical variable in question. Figure 4(*b*) shows two such energy profiles for the chemical states A and B.

The landscape determines the kinetics of the chemical reactions, and similarly the kinetics, if measurable, can be used to reconstruct the landscape. For molecular motors, chemical reaction rates depend strongly on the spatial position of the motor. Certain transitions are probable only at certain positions, and the interdependence of chemical kinetics and mechanical energy profiles determines many critical components of the motor such as torque-speed curves, maximum velocity, maximum torque, turnover, efficiency and reversibility. The system of discrete chemical states with energy profiles and rate constants that depend on the continuous mechanical variable(s) can be represented by *reaction-diffusion* or coupled

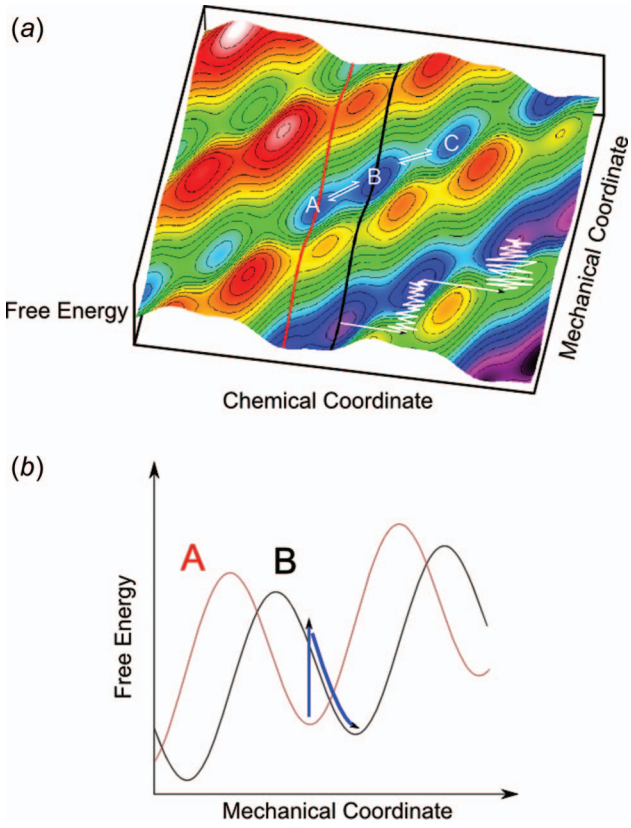

Figure 4. (*a*) Simplified two-dimensional energy landscape with one chemical and one mechanical coordinate. The white path shows the diffusing path of the motor as it fluctuates within and between mechanochemical states, defined by wells in the landscape and labelled A, B, and C. The periodic nature of the landscape reflects the periodicity of the chemical cycle, and as the chemical cycle is completed there is also motion towards the top along the mechanical coordinate. The white path in the lower right of the landscape shows a motor making rapid chemical transitions and slow diffusing mechanical relaxations moving between states A, B, and C. (*b*) Sections of the landscape at fixed values of the chemical coordinate represent energy profiles of distinct chemical states, as used in Brownian Dynamics. Two such energy profiles for sections through states A and B, marked by the red and black lines in (*a*), are shown here. The motor operates by making fast chemical transitions at fixed mechanical postions followed by relaxation of the motor along the new energy profile, as indicated by the blue arrows shown in (*b*). Equivalent sections at fixed values of the mechanical coordinate would represent the chemical kinetics for any given mechanical state. Applying an external load on the motor constitutes tilting the landscape along the mechanical coordinate. For further equations and Langevin descriptions of the landscape of a rotary motor, see [26].

Langevin equations [26], which are usually solved numerically to give either average probability densities or simulated motor trajectories. Xing et al. have built a Brownian Dynamics model to describe torque generation in the BFM [27], which we will discuss in further detail in Section 3.3.

3. Measuring rotation of the bacterial flagellar motor

3.1. Experimental methods

To understand the mechanism of the BFM we need to measure its motion. We want to use information about the torque and speed of the motor to reconstruct attributes such as energy profiles and state transitions so that we may examine the underlying torque-generating mechanism. To do this we need to be able to measure with high precision the position of and torque applied to the rotor. This is an example of *single-molecule* biophysics. Although the BFM contains hundreds of thousands of atoms, the label *single-molecule* is still applied to experimental measurements of single BFMs; partly because the experimental and theoretical techniques are the same as those used on smaller molecular motors, and partly because the atomic precision of protein structures distinguishes even a large protein complex like the BFM from objects made of bulk materials, in which the exact position of individual atoms is neither specified nor important.

How can we measure the rotation of a single BFM? The main techniques for imaging objects on the nanometre length-scale, electron microscopy and X-ray crystallography, both require very dead samples, so neither is appropriate for live recording of any molecular motor. Atomic force microscopy (AFM) is promising, but molecular motor studies to date using AFM have been limited to purified motors isolated on flat surfaces, and it may be a long time, if ever, before AFM develops to the point where it can be used to monitor the BFM in live cells. This leaves light microscopy. The motor itself is too small to observe in visible light, and so a visible marker must be attached to a part of the motor that rotates. The earliest demonstration of BFM rotation was achieved using tethered cells by Silverman and Simon in 1973 [28]. Flagellar filaments were fixed to the glass surface of a microscope coverslip and the cells rotated around these fixed tethers. This demonstrated that the motion of the BFM was rotational, not oscillatory. The marker attached to the rotor in this case was the micron-sized cell body of *E. coli* itself, easily observable with video microscopy.

In the standard modern version of this experiment, known as a *bead assay*, we attach a polystyrene bead to a truncated filament of a cell body fixed to the surface of a coverslip. The bead can be varied in size and each size has a well-defined viscous drag-coefficient. The rotation of the marker can be detected by many methods. The most straightforward is to image it using dark-field or bright-field microscopy with a fast camera, and track its rotation in recorded video. It is worth pointing out here that the Rayleigh criterion (or other similar criteria) for optical resolution is irrelevant here. What we need to do is to determine the position of the image of a *single* object, not to resolve the separation of two separate objects. By fitting the image to a 2D Gaussian or other empirical function, offsets in the centre of this function can be determined with arbitrary accuracy, depending only on the number of photons collected to form the image (which in turn determines the precision of the fit). The slower and brighter the object being tracked, the greater the position sensitivity. For example, single fluorescent molecules are typically tracked with frame rates on the order of $1\ s^{-1}$ and corresponding spatial precision of ~ 1 nm. Brighter objects can be tracked with more temporal and spatial resolution, and a trade-off always exists between faster frame rates and better spatial resolution in each frame. A less computationally intensive method, and our standard method, is to detect the rotation of the bead by using an *optical trap*, invented by Ashkin et al. in 1986 [29]. An optical trap uses light with a Gaussian intensity profile passing through a bead of higher refractive index than its surroundings to form a harmonic potential and exert force on the bead. Rather than using a strong laser and an optical trap to exert and measure force, we use a weak laser focused on the bead for position detection. Any small change in the position of the bead is measured by an associated shift in the direction of the laser light scattered by the bead. This is measured using a quadrant photodiode (QPD, a set of four photodiodes each covering a single quadrant) located in an optical plane conjugate to the back focal plane of the condenser lens that collects the laser light after it has interacted with the bead. A schematic of our apparatus is shown in Figure 5.

The invention of optical trapping allowed researchers to exert pico-Newton forces and measure displacements of nanometres with sub-millisecond time-resolution. This made it possible to perform single molecule measurements on molecular motors at their natural length, time and energy scales. Spatial resolution of bead displacement is limited by the width of the beam waist in the specimen plane which is related to the wavelength of the laser light and, for an overfilled objective, the numerical aperture (NA) of the objective. For small beads of diameter d, and for displacements much smaller than the laser focus, the response of the QPD was experimentally verified to be proportional to $(d/\omega_o)^3$ by Gittes and Schmidt [30]. In the case of our experiments this allows us to measure beads from as small as 200 nm up to as large as 2000 nm using a 632 nm HeNe laser and a $100\times$ immersion-oil

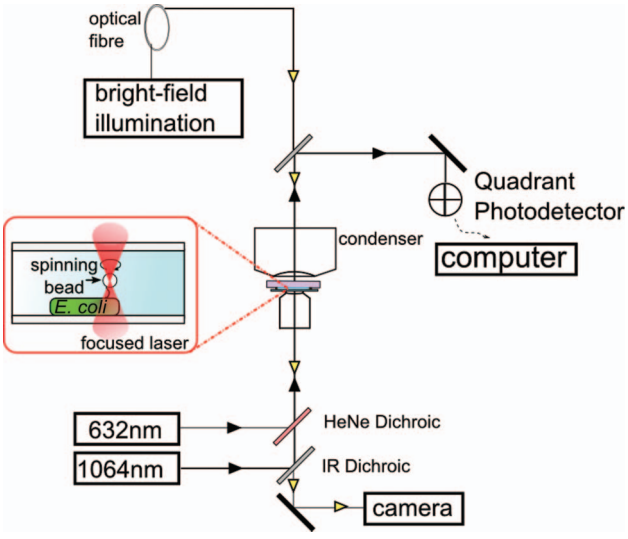

Figure 5. Schematic of a dual optical trap apparatus showing the standard bead assay. The polystyrene bead is attached to a filament stub of an *E. coli* cell fixed to the surface of a coverslip (by flowing a solution of beads over a surface decorated with cell bodies). The excess beads are washed out and the slide is sealed and placed on a microscope. The spinning beads can be seen on a video camera, and their position can be resolved to high precision by looking at the change in scattering of the laser light with a quadrant photo-diode. This microscope has two optical traps so that lasers of different wavelengths can be used to track beads of different sizes.

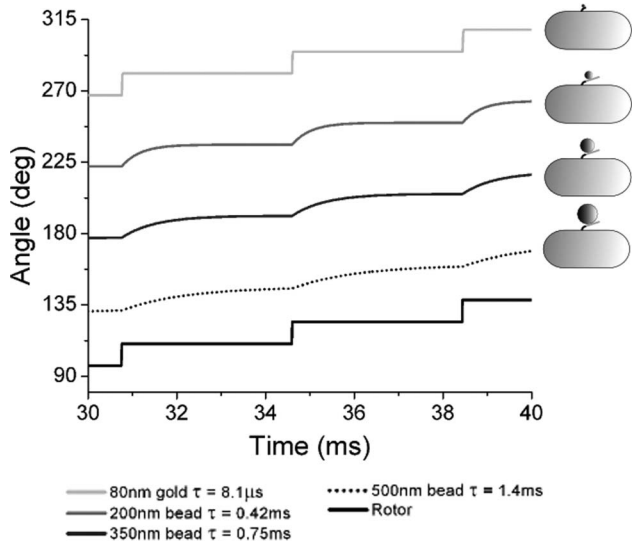

Figure 6. This figure shows schematically the difference in response time for different size loads. Four different loads are shown; 80 nm gold beads attached directly onto the hook, 200, 350, and 500 nm polystyrene beads attached to truncated filaments. The relative sizes of the markers to the filament and the cell are shown to scale in diagrams adjacent to each trace. The relaxation times are derived from known hook stiffness and drag coefficients for each size bead. The trace in black at the bottom of the figure is the stepping motion of the rotor, and the traces above are the response curves of the marker, each offset by 45° for clarity. The response is 'smoothed' due to the soft linker of the hook and depends on the size of the load. The rotor step is 13.8° as observed by Sowa et al. [32] and the motor is spinning at 10 Hz.

objective with NA 1.30. By altering the size of the bead, the viscous drag coefficient can be varied and thus the performance of the BFM under different torque regimes can be explored.

Our observations of the motor are limited by the need to use a comparatively large marker. For a motor rotating a large bead there is a time-scale separation between the positions of the motor and the bead. This separation allows the motor to work with very high Stokes efficiency, i.e. most of the electrochemical free energy is used to drive the viscous load rather than being dissipated directly as heat [31]. The elastic linker of the hook is soft enough to allow the rotor to fluctuate over several steps before the load moves noticeably and similarly work done to stretch the linker can be returned to the motor before it is dissipated by moving the load. Thus, the hook effectively smooths the discrete stepped motion of the rotor. At high speed and low load, the tension between the load and motor relaxes faster, and the motor works against a smaller elastic load. The characteristic smoothing time decreases along with the load, and so small loads allow us to look more closely at the details of the rotor's motion. The change in response time for different size beads is shown in Figure 6.

Recently we have been able to extend our experiments to lower load regimes using a dark field microscope and gold particles attached directly to the hook. Dark field microscopy has been used to detect rotation in F_1-ATPase by Yasuda et al. [33]. They used forward-scattered light from a 40 nm gold particle attached to the rotating gamma subunit of F_1-ATPase. The scattered light from the gold particle was collected on a high speed camera. In our experiments we use a slightly different dark field microscope where the laser passes through the objective and illuminates the gold beads from below. The back-scattered light is then collected at an even higher speed camera (109 kHz), and positions can be determined with nanometre precision at this frame rate. Gold beads are attached directly onto the hook, so the additional drag of the filament stub is also removed [34].

3.2. *Energetics of the bacterial flagellar motor*

The wild-type BFMs of *E. coli* and many other species are powered by H^+ ions (protons). Several other

species, including the marine bacterium *Vibrio alginolyticus*, have BFMs powered by Na^+ ions [35]. The stator proteins in the Na^+-driven motor of *V. alginolyticus* are called PomA and PomB, and are structurally similar to MotA and MotB from *E. coli*. Based on this similarity, a chimeric fusion protein known as PotB, combining parts of PomB and MotB, was made by Asai et al., and combined with PomA to make a Na^+ driven chimeric motor that works in *E. coli* [36]. The sodium-motive force (SMF) of *E. coli* can be changed without drastically affecting cell function, unlike the proton-motive force (PMF) which is closely regulated and linked to pH. (Extremes of pH change the charge state of ionisable groups on the surface of proteins, and therefore usually have severe effects on protein folding and function.) Controlling the SMF in cells with chimeric motors has allowed the dependence of flagellar rotation on each component of the IMF to be explored.

In order to control the SMF for experiments on the chimeric motor, we developed fluorescence microscopy methods to measure either the internal sodium concentration or the membrane voltage in single, live, *E. coli* cells [37]. We found the following dependence of membrane voltage and the sodium chemical potential in cells with chimeric motors:

$$V_m(\mathrm{mV}^{-1}) \approx 57 - 28\ \mathrm{pH},$$
$$(\Delta\mu/q)(\mathrm{mV}^{-1}) \approx 5 + 5\ \mathrm{pH} - 47\log_{10}\ [\mathrm{Na}^+],$$

where pH and $[Na^+]$ are the pH and sodium concentration in mM of the medium surrounding the cell. Thus, to a reasonable approximation the membrane voltage depends on pH, but not $[Na^+]$, and the chemical potential depends on $[Na^+]$ but not on pH. This allows independent control of the two components of SMF. The chimeric motor rotated stably for all combinations of pH between 5 and 7 (corresponding to V_m between ~ -80 and -140 mV) and $[Na^+]$ between 1 and 85 mM (corresponding to $\Delta\mu/q$ between $\sim +30$ and -50 mV).

3.3. *Torque versus speed*

Finding the relationship between torque and speed is a means to quantify the mechanochemical cycle of any motor. In the case of the BFM the torque on the motor can be adjusted by changing the size of the bead used as the marker. Larger beads have larger drag coefficients and result in the motor operating at higher torque. The drag coefficient can also be changed by varying the viscosity of the medium while observing the same bead and motor [38]. This is important when small beads are used, as it allows the viscous drag coefficient of the truncated flagellar stub, similar to that of a 0.2 to 0.3 μm bead, to be quantified [39]. Torque-speed curves obtained for wild-type and chimeric motors in *E. coli* using these methods as well as *electrorotation* (see figure legend) are summarised in Figure 7.

What can we tell by looking at this relationship? First we can see the maximum speed of the motor, which is the zero-torque speed. We can also see the stall torque, which is the y-intercept in Figure 7. The other key features of the torque–speed curve are the plateau at low speed and the steeper linear regime at high speed. Where these two regimes intersect is known as the 'knee' of the torque–speed curve. The continuity of the plateau regime on either side of stall shows that there is no irreversible step in the mechanochemical cycle. If such a step did exist, the torque would be expected to increase sharply before the motor could be forced backwards [41]. The 'plateau' is a region of constant torque at high load where the motor is rate limited by the mechanical relaxation of the bead, as shown in Figure 6. After the 'knee', the torque decreases linearly to zero as the motor moves faster. At low loads the motor is rate limited by kinetic rate constants in the mechanochemical cycle, for example the arrival, binding or transit of ions. Evidence for this is shown by the large effect of temperature and isotope substitution on the speeds at low load, compared with the small effect of these changes at high load [40,42]. At high and low loads the speed varies linearly with the PMF [43].

Any model that hopes to explain the torque generating mechanism of the BFM has to be able to reproduce the observed torque–speed relation. We outline two models: a fully kinetic model from Berry and Berg in 1999 [44], and a reaction-diffusion model from Xing et al. in 2006 [27]. Berry and Berg used a minimal three state kinetic model. Each step in the cycle is assigned a chemical free energy change, U_i, and also rotation of the rotor through some angle φ_i. If φ is the angle moved in one cycle and β_i is the fraction moved in step i, the motor performs work $W_i = \varphi_i\Gamma = \beta_i\Gamma\varphi$ in step i, where Γ is the torque. The sum of all U_i must be equal to $nq \cdot \mathrm{PMF}$, where n is the number of protons transiting the membrane per cycle, q is the charge of a single proton, and PMF is the proton-motive force. Similar to β_i, a second set of parameters, α_i, are defined as the fractions of the free energy from proton transit that are dissipated as heat, or used to do work, in step i, so that $U_i = \alpha_i nq \cdot \mathrm{PMF}$. A third parameter for each step, k_i, determines the absolute rate of each step, and rate constants are given by

$$k_{fi} = k_i \exp\left(\frac{U_i - W_i}{2kT}\right)$$

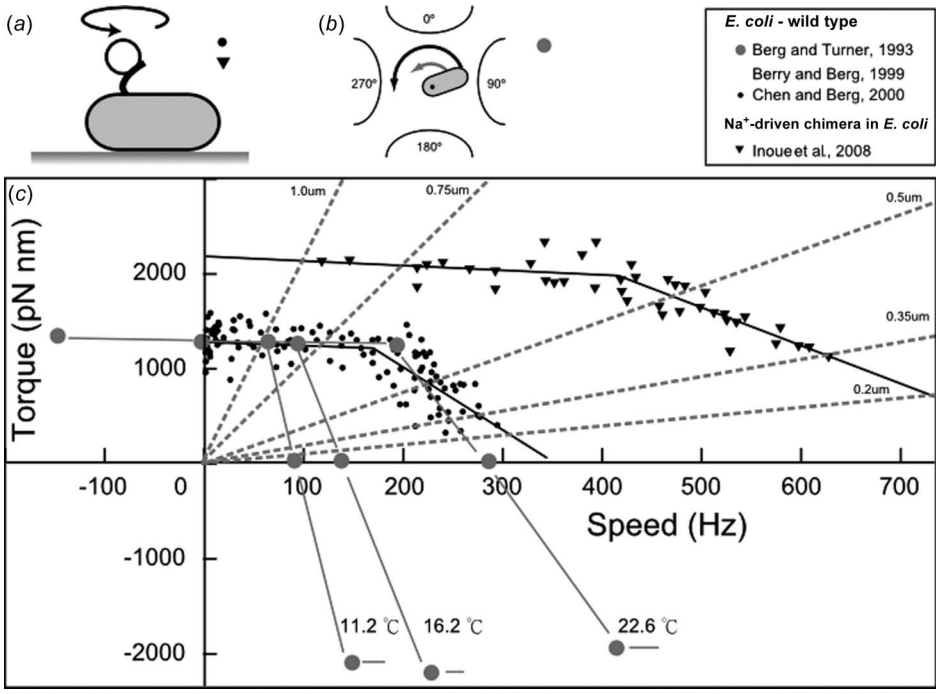

Figure 7. Torque–speed curves for the proton powered wild-type *E. coli* and for Na^+-driven chimera at full induction (maximum number of stators). (*a*)–(*b*) Methods of measuring torque–speed relations. (*a*) Beads attached to flagella. The size of the bead or the viscosity can be changed to vary the load and thus the torque of the motor. Load lines for six different sizes of beads in aqueous buffer are shown on the plot as dashed grey lines, for beads from 1.0 to 0.2 μm. (*b*) Electrorotation of tethered cells [40] – microelectrodes generate a MHz rotating electric field at the cell which applies an external torque (black arrow) that adds to the motor torque (grey arrow). In this way the torque speed relation can be explored for motors forced to rotate in reverse, or forwards faster than the zero-torque speed. (*c*) Torque–speed relationships for flagellar motors using different methods. The *E. coli* wild type torques are shown by circles, with the electrorotation torque–speed measurements shown using grey circles, and the Na^+-driven chimera torques by black triangles. Figure adapted from Sowa and Berry [11]. Reprinted with permission from Q. Rev. Biophys., 41 (2008), pp. 103–132. Copyright (2008) by Cambridge University Press.

and

$$k_{bi} = k_i \exp\left(\frac{-(U_i - W_i)}{2kT}\right)$$

for the forwards and reverse rates of step i, respectively. These expressions assume for simplicity that U_i and W_i each affect the forward and reverse rate constants symmetrically. With torque and PMF specified, solution of the coupled linear ordinary differential equations for the occupancy probabilities of each kinetic state, assuming steady state, gives the flux around the mechanochemical cycle and thus also the rotation speed. A brief exploration of the parameter space of this model is shown in Figure 8.

Some of the assumptions in this model are no longer valid. It assumes that either one or two protons are translocated in each mechanochemical cycle, that there are eight stators, and each stator completes 120 cycles per revolution. Current understanding is that the up-to-11 stators [15] each probably complete 26 cycles per revolution (see Section 3.4). Changing these values, however, does not affect the model's prediction of the shape of the torque–speed relationship. We are working on a more general kinetic model which will be used to fit newly measured torque–speed relationships of the chimeric BFM at 25 different combinations of V_m and $\Delta\mu$. The model is based on a four state model and has more than 20 free parameters which allow it to span all possible combinations of the rate constants and their dependences upon torque and either component of the SMF. The advantage of kinetic models such as these is that they are simple and therefore fast to compute, allowing automated searching of the multi-dimensional parameter space to find good fits to the experimental data. Despite their lack of mechanical detail, kinetic models substantially constrain possible models of the motor mechanism.

Xing et al. [27] proposed a reaction-diffusion model which was designed to ensure that motor rotation and ion transport are tightly coupled. Figure 9 shows energy profiles (potentials of mean force versus rotor-stator angle, equivalent to those shown in Figure 4(*b*)) for two states of a single model stator. Transitions between state 1 (solid lines) and state 2 (dashed lines) are coupled to the motor binding two ions from outside the cell, and are

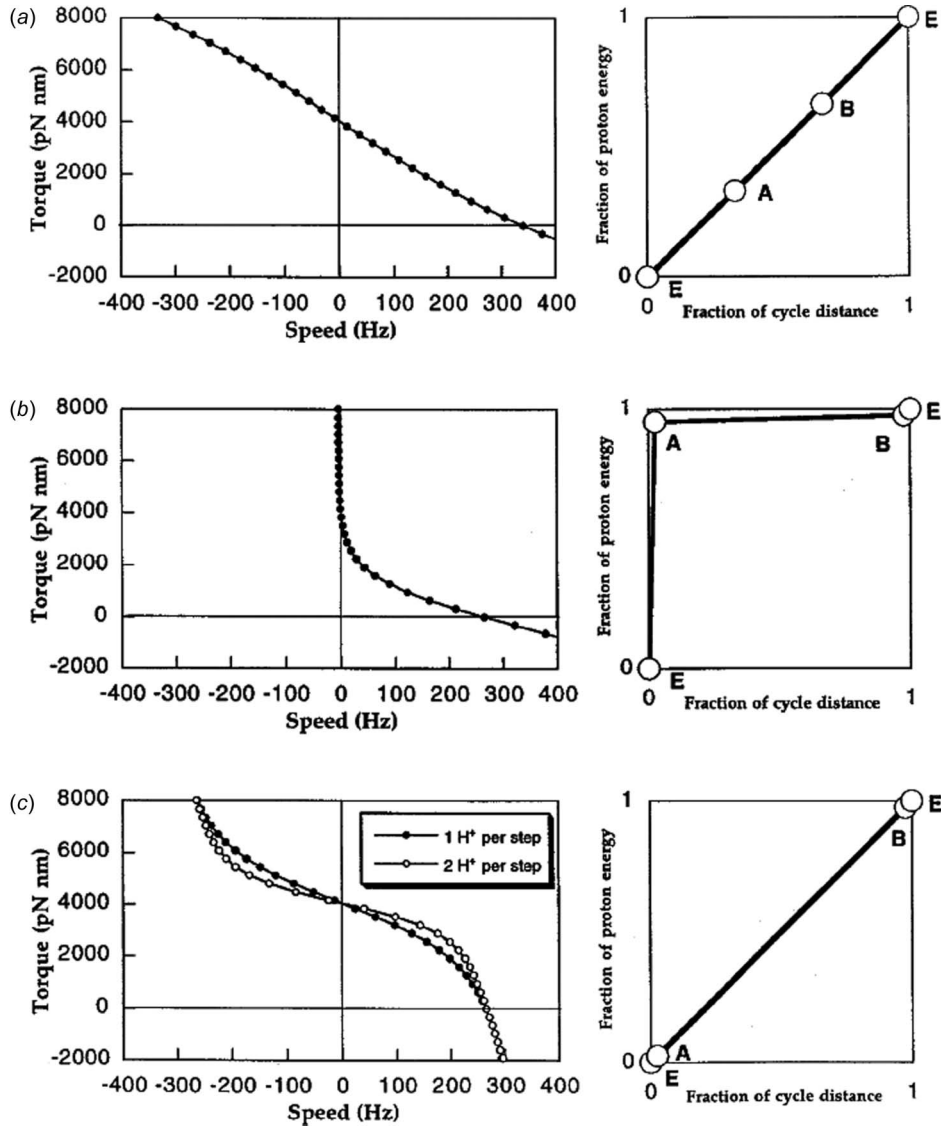

Figure 8. The torque–speed relationship for the kinetic model described in the text from Berry and Berg [44]. The right-hand panels are a graphical representation of the parameter sets, showing the degree to which each step of the cycle dissipates the available free energy and results in motor rotation. (*a*) The torque speed relation when all three steps in the cycle are equivalent, with parameters: $\alpha_1 = \alpha_2 = \alpha_3 = \beta_1 = \beta_2 = \beta_3 = 1/3$, $k_1 = k_2 = k_3 = 6 \times 10^4\ s^{-1}$. (*b*) The dissipation of proton free energy, and the rotation occur in nearly entirely separate steps, with parameters: $\alpha_1 = \beta_2 = 0.95$, $\alpha_2 = \alpha_3 = \beta_1 = \beta_3 = 0.025$, $k_1 = k_2 = k_3 = 10^5\ s^{-1}$. (*c*) If the dissipation of the proton free energy and the rotation of the rotor happen in a single step the torque–speed relation predicted by the model looks qualitatively similar to the experimentally observed torque–speed curve. Parameters: $\alpha_2 = \beta_2 = 0.95$, $\alpha_1 = \alpha_3 = \beta_1 = \beta_3 = 0.025$, $k_1 = k_2 = k_3 = 10^5\ s^{-1}$ (*closed circles*); $k_1 = k_2 = k_3 = 4.2 \times 10^4\ s^{-1}$ (*open circles*). Taken from Berry and Berg [44]. Reprinted with permission from Biophys. J., 76 (1999), pp. 580–587. Copyright (1999) by Elsevier.

possible only at angles corresponding to the upper shaded area. Ion transit is completed by release of the two ions into the cell, which in turn is possible only at the angles indicated by the middle shaded area. The lowest shaded area shows the start of the next cycle of the motor. The linear sections of the energy profiles are chosen to produce constant torque in the plateau region. The peaks in the profiles were found to be necessary to prevent slipping, for example when the system moves over the top of a 'tooth' in a single potential, leading to rotation uncoupled from the chemical state transition. The coupling to two ions at a time was introduced to ensure that enough free energy is available in a single step of 1/26 of a revolution to generate the measured torque of the motor at low speeds – this point is discussed in more detail in Section 3.4 below. Otherwise, the two-state kinetic cycle and the potentials were chosen to be as simple as possible, reflecting the limited structural and

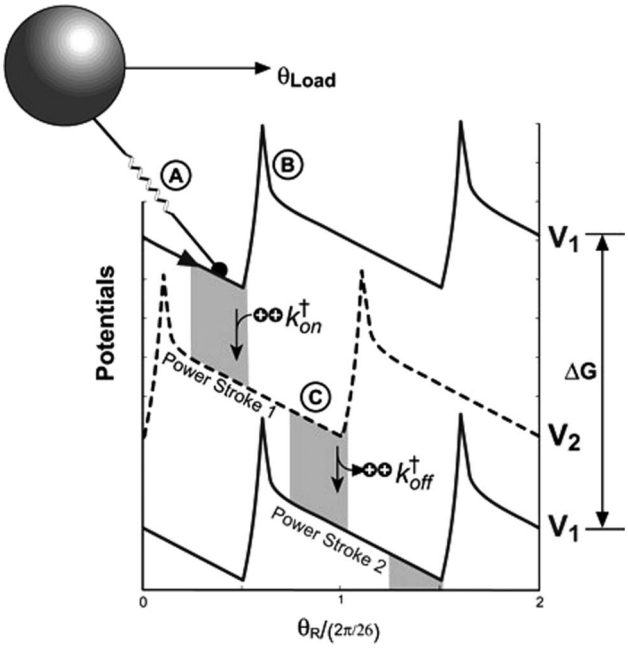

Figure 9. The Brownian Dynamics model of Xing et al. [27]. The energy potentials in each of two chemical states of a single stator are modelled as identical periodic piecewise linear functions offset by half a period. The 26-fold periodicity reflects the structure of the FliG ring in the rotor and the observation of 26 steps per revolution (Section 3.4). Each transition between the two potentials initiates a power stroke, which is modelled as a constant torque. The soft linker between the rotor and the load is indicated by the spring, A. The sharp peaks in the potential labelled B prevent thermal fluctuations from causing back-steps that are uncoupled from the chemical transitions, thus ensuring tight coupling between rotation and proton flux. Each motor cycle transports two ions from periplasm to cytoplasm, which decreases the free energy of the system by $2q \times$ PMF and advances the rotor by $2\pi/26$. The (shaded) transition regions specify the positions where the transitions between the potentials can take place. Figure taken from Xing et al. [27]. Reprinted with permission from Proc. Natl. Acad. Sci. USA, 103 (2006), pp. 1260–1265. Copyright (2006) by the National Academy of Sciences.

kinetic data available to constrain the model. The angle θ of the rotor relative to a single stator obeys the Langevin equation:

$$\zeta_M \frac{d\theta}{dt} = -\frac{\partial}{\partial\theta} V_M(\theta, s) - \kappa(\theta - \theta_L) + [2k_B T \zeta_M f_M(t)]^{1/2},$$

where ζ_M is the drag coefficient of the rotor, V_M is the energy potential of mean force along the minimum energy path described as a function of θ, s is a binary variable describing the state of the stator, κ is the spring constant of the link to the bead and θ_L is the angle of the bead. The last term is the stochastic Brownian force acting on the stator, where $f_M(t)$ is uncorrelated white noise. The slope of V_M determines the force profile the stator exerts on the rotor. Motors with multiple stators are modelled by replacing V_m with a potential which is the sum of the potentials from all stators. A similar Langevin equation describes the motion of the bead, but without the V_m term.

Numerical analysis and simulations of this model confirmed that for a motor dragging a large load, there is a time-scale separation between the motor and the load dynamics, in addition to the *a priori* assumed timescale separation between the motion of the rotor and the chemical transition time. The soft linker allows the motor to work against an approximately constant conservative torque, similar to the situation illustrated in Figure 4. For large loads, this torque slows the rotor to the point where chemical transitions are almost certain to occur before the rotor has moved beyond the low-angle part of the allowed transition zone in Figure 9, where the torque is constant. This produces the plateau region of the torque–speed curve. By contrast, for small loads the bead relaxes much faster and there is a significant probability that the rotor will reach the minimum of an energy profile before a chemical transition takes the system to the next state. Since the average torque at the minimum is zero, this produces a steeply decreasing motor torque as the load is decreased and the speed approaches the zero-load speed. The success of this model consists of explaining the experimentally observed sharp transition between these two regimes at the 'knee', as shown in Figure 10.

The same authors revisited this model [45] in 2009. They added compliant springs linking the stators to the cell wall, to explain the most recent results from Yuan and Berg [46]. The original model predicted that the zero-load speed would actually *decrease* with increasing number of stators, as coordinated transitions in all stators were required for the rotor to rotate. Yuan and Berg found a lack of dependence of zero-torque speed on stator number, which implies that competing stators do not impede each others' interaction with the rotor. Stator springs allow each stator to step independently, storing energy in stretching its own spring, rather than requiring the rotor-stator angles of all stators to change in synchrony. The stator-spring model can also reproduce the experimentally observed stepping behaviour, and was used to predict dwell time distributions between steps as well as a variety of possible dependences of stepping patterns upon the number and relative anchorage points of separate stators. These predictions will be tested by future experiments in our group, as discussed in Section 3.4 below.

3.4. *Stepping rotation*

Molecular motors operate on periodic tracks and with periodic chemical cycles. The consumption of a

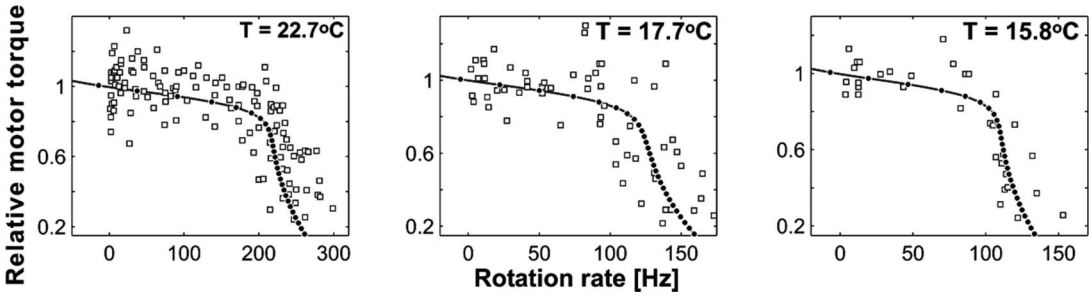

Figure 10. Comparison of model predictions from Xing et al. [27] (dots and lines) with experimental data [38] (squares), for torque–speed curves at different temperatures. Figure taken from Xing et al. [27]. Reprinted with permission from Proc. Natl. Acad. Sci. USA, 103 (2006), pp. 1260–1265. Copyright (2006) by the National Academy of Sciences.

discrete number of fuel molecules per cycle, and the repetition of a track unit implies that at some fundamental level there are discrete mechanical steps where torque or force generation occurs. Observing this quantised movement we can look beyond torque–speed curves to obtain a more detailed picture of the motor mechanism. For example, kinesin was first observed to step in 1993 by Svoboda et al. [47]. They used an optical trap to monitor the position of a silica particle attached to a kinesin molecule walking along a surface-bound microtubule. This was the first observation of discretised molecular motion and they saw 8 nm steps corresponding to the 8 nm α-β-tubulin structural repeat of the microtubule track. Further experiments confirmed that each step uses one molecule of ATP [48]. Rotational motion of F_1-ATPase was first observed in 1997 by Noji et al. [24]. They showed that F_1-ATPase rotates in three distinct 120° steps, each of which is linked to the binding, hydrolysis and release of a single ATP molecule [49]. The three-fold symmetry of the track, with three pairs of α and β subunits arranged in a hexagon, was reflected by the presence of three steps per revolution. This was followed in 2001 by Yasuda et al. [33] discovering substeps within this rotation using a dark field microscope and a high speed camera. They were able to see two substeps of 80° and 40°. From an analysis of these substeps and adjusting the ATP concentration they were able to determine which substeps corresponded to which parts of the chemical cycle. In particular the 80° substep was driven by ATP binding and the 40° substep by release of hydrolysis products.

For the BFM, the $\sim$26-fold periodicity of the FliG ring in the rotor [50], implies a discrete torque generating step at the heart of motor function. Indirect evidence for a stepping mechanism was found by Samuel and Berg [51]. They performed a fluctuation analysis which observed a quadratic relationship between the mean and variance of rotation speeds, a predicted result for any mechanism involving a Poisson stepper with exponentially distributed dwell times. In a further analysis of variance and speed they predicted 50 steps per revolution per stator [52].

Due to the high speed rotation of the BFM under standard biological conditions only recently has sufficient experimental resolution been available to observe stepping in the BFM. The smoothing of the signal by the hook means that the intervals between steps must be larger than the relaxation time of the bead if steps are to be seen. The drag coefficient can be reduced as discussed earlier by using smaller beads, but this leads to faster rotation, and thus requires greater time resolution. The spring constant of the hook has been measured by Block et al. [53] to be $\sim$400 pN nm rad^{-2} and the subsequent damping of the bead motion is equal to the viscous drag on the bead divided by the spring constant of the hook. Effectively this means that for 0.5 μm beads the rotation speed needs to be less than 12 Hz for the steps to be observable.

In 2005 we first observed steps in the BFM [32]. Sodium driven chimeric motors in *E. coli* were kept at low stator number by controlling the amount of stator protein made in the cells, and the SMF was reduced so that the speed of the motor was kept below 10 Hz, enabling discrete steps to be observed as shown in Figure 11. The steps were measured using two different methods. The first method was using a laser focused on a 500 nm polystyrene particle attached to a truncated filament as in our standard bead assay. In this case, the SMF was reduced by lowering the external Na^+ concentration to 0.1 mM, although at the time the relationship between SMF and Na^+ concentration was not known. The second method was using high-speed video of 200 nm fluorescent beads attached to rotating truncated filaments. In this case, cells were illuminated with a high-intensity mercury arc lamp at 475 nm bandpass, which was thought to reduce the membrane voltage, and thus the SMF, by unspecified mechanisms of photodamage.

Both methods showed 26 steps per revolution, and a corresponding step size of 13.8°, in agreement with the periodicity of the ring of FliG in the rotor. If steps

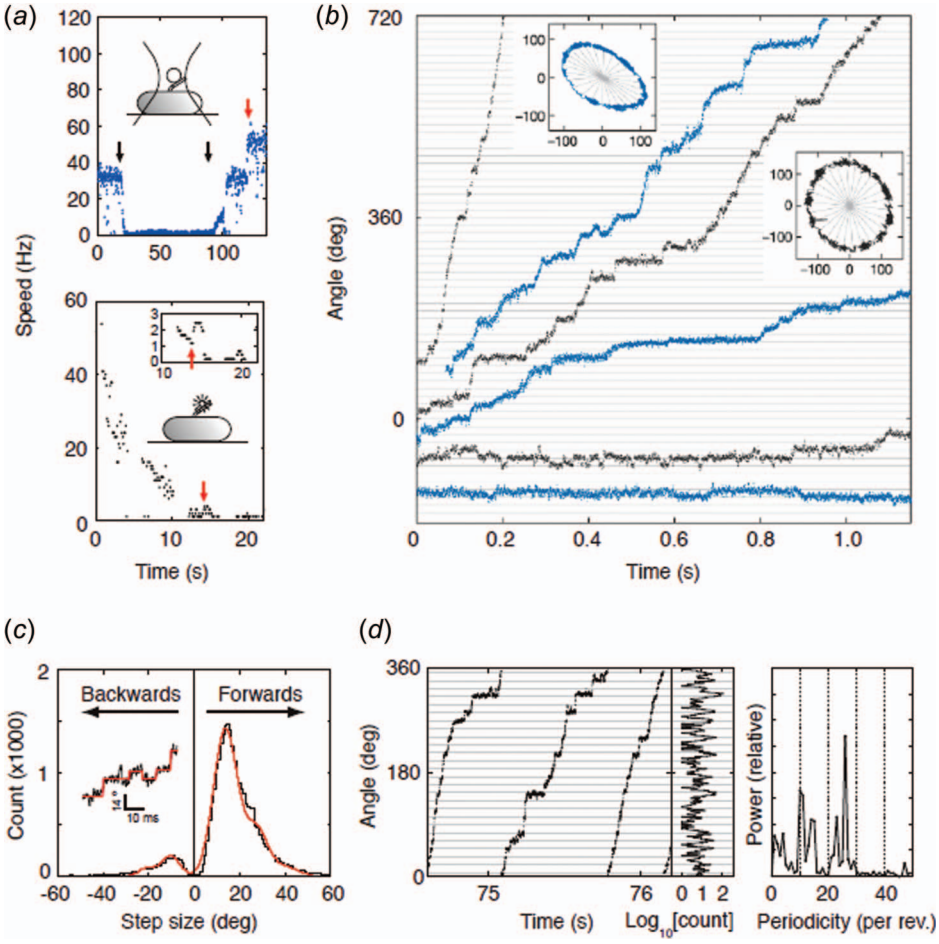

Figure 11. Steps in slow flagellar rotation. (*a*) Reducing SMF and motor speed of a chimeric Na^+-driven flagellar motor in *E. coli*; upper: by lowering external Na^+ concentration (5 to 0.1 mM and back, black arrows) and lower: by photodamage. The speed doublings marked by red arrows indicate a change from one to two stators. (*b*) Stepping rotation of flagellar motors with a range of average speeds depending on different SMF. Insets show the positions of beads attached to flagellar filaments, scales in nanometres. Horizontal and radial lines indicate (1/26 rev). (*c*) Step size distribution (black) with multiple Gaussian fit (red). The peak of forward steps is 13.7°, indicating 26 steps per revolution. An example of steps identified by a step-finding algorithm is shown (inset). (*d*) Plot of angle against time during three revolutions, a histogram of dwell angles for the same revolutions and the power spectrum of that histogram. The peak at 26 per revolution corresponds to a step size of 13.8°, and shows that the motor stops at the same angles on successive revolutions. Speeds shown in black were measured using optical interferometry, those in blue using high-speed fluorescence microscopy (insets in (a)). Figure reproduced from Sowa et al. [32]. Reprinted with permission from Nature, 437 (2005), pp. 916–919. Copyright (2005) by Nature Publishing Group.

of 13.8° are the smallest unit of movement in the BFM then using energy balance it should be possible to calculate the number of ion transits that correspond to a step. The stall torque for the chimera sets an upper bound to the step size per single ion transit. Under standard conditions ($[Na^+]_{ex} = 85$ mM and pH 7) SMF is -150 mV and the average torque per stator unit is 150 pN nm to rotate a 1 μm bead [37]. From this the upper bound to step size can be calculated to be 10° per step, or 36 ions per revolution. This corresponds to the 35-fold symmetry of the C ring, but implies that each step at high load, if tightly coupled, requires more than one ion transit, but less than two. The problem of dividing 38 ions into 26 steps, while retaining tight coupling, requires new models and further experiments. We can imagine two simple solutions: either the motor is tight coupled and the stall-torque estimation is incorrect, or rotation is not tightly coupled to proton translocation and the model of Xing et al., which uses two ions per step, must be altered to allow slipping. A third, outside, possibility is that the mechanochemical cycle and the observed steps are not the same thing. This would require an elastic link between the site of torque generation (tight coupled, ~36 ions per rev, presumably the bottom of the C-ring) and, in series, another site with a 26-fold interaction potential between the rotor and stator that produces the observed steps

(presumably the FliG ring at the top of the C-ring). The rotor structure has a region of low density between the two parts of the C-ring that would be a candidate for the elastic link, but before taking such a model seriously it will be necessary to rule out other simpler explanations, and to find a signature for such a mechanism in more detailed analysis of motor stepping. We are currently trying to obtain the relevant data using our dark-field microscope and gold beads attached directly to hooks. The high time resolution of this system allows us to resolve steps at motor speeds in excess of 200 Hz. Combined with our new ability to control both components of the SMF, we hope to be able to make a detailed statistical examination of the stepping of the BFM and investigate the details of the mechanism, including the question of possible stepping coordination of multiple stators acting on the rotor.

4. Conclusion

Biological molecular motors show us how directed motion can be generated by nanometre-scale devices working at the energy scale of the thermal bath. Direct and indirect observations of functioning single motors allow us to see fundamental processes of statistical physics unfolding in microscopic detail at room temperature, something that was unimaginable only a few decades ago. The bacterial flagellar motor is the largest of several molecular motors that have been extensively studied, revealing their mechanisms in ever greater detail. Understanding how these machines work is fascinating to the modern, interdisciplinary physicist. Perhaps more fascinating still will be the next challenge, to try and build something for ourselves that works in the same way. Evolution has given natural biological motors a big head-start, but we have reached the stage where we can contemplate beginning to catch up.

Acknowledgements

The authors would like to thank Richard W. Branch for his many critical readings of the manuscript and subsequent comments.

Notes on contributors

Matthew Baker is an Australian D.Phil. student at Oxford University in Dr Berry's Rotary Molecular Motors Group. He completed his Honours degree in Physical Chemistry studying the Fluctuation Theorem with Professor Denis Evans and Dr Edie Sevick at the Australian National University, Canberra in 2004. He was awarded a General Sir John Monash Award in 2005 and used this funding to work first on kinesin with Professor Christoph Schmidt at the Vrije Universiteit in Amsterdam, and then to move to Oxford University. He is currently completing his D.Phil. thesis investigating the effects of temperature on the function of the bacterial flagellar motor.

Richard Berry completed undergraduate and graduate Physics degrees at Oxford University in 1989 and 1993. After a short postdoc investigating theoretical models of HIV infection, he began experimental investigation of the Bacterial Flagellar Motor in 1994, as a Wellcome International Travelling Prize Research Fellow in the lab of Howard Berg in the Department of Molecular and Cellular Biology at Harvard. After spending time in Oxford Biochemistry (with Judith Armitage) and King's College London (with Bob Simmons), he started his current research group in Oxford Physics in 2000.

References

[1] B. Alberts, A. Johnson, J. Lewis, M. Raff, K. Roberts, and P. Walter, *Molecular Biology of the Cell* [Book and CD-ROM], Garland Science, London, 2002.
[2] S.M. Block, *Fifty ways to love your lever: myosin motors*, Cell 87 (1996), pp. 151–157.
[3] M.A. Geeves and K.C. Holmes, *Structural mechanism of muscle contraction*, Annu. Rev. Biochem. 68 (1999), pp. 687–728.
[4] J.C. Haselgrove, M. Stewart, and H.E. Huxley, *Cross-bridge movement during muscle contraction*, Nature 261 (1976), pp. 606–608.
[5] I.H. Riedel-Kruse, A. Hilfinger, J. Howard, and F. Julicher, *How molecular motors shape the flagellar beat*, HFSP J. 1 (2007), pp. 192–208.
[6] A.I. Tauber, *Metchnikoff and the phagocytosis theory*, Nat. Rev. Mol. Cell Biol. 4 (2003), pp. 897–901.
[7] D.N. Dao, R.H. Kessin, and H.L. Ennis, *Developmental cheating and the evolutionary biology of Dictyostelium and Myxococcus*, Microbiology 146 (2000), pp. 1505–1512.
[8] T.D. Pollard and W.C. Earnshaw, *Cell Biology*, W.B. Saunders, Kidlington, 2002.
[9] D. Cyranoski, *Swimming against the tide*, Nature 408 (2000), pp. 764–766.
[10] C.M. Rosenberger and B.B. Finlay, *Phagocyte sabotage: disruption of macrophage signalling by bacterial pathogens*, Nat. Rev. Mol. Cell Biol. 4 (2003), pp. 385–396.
[11] Y. Sowa and R.M. Berry, *Bacterial flagellar motor*, Q. Rev. Biophys. 41 (2008), pp. 103–132.
[12] G.L. Hazelbauer, J.J. Falke, and J.S. Parkinson, *Bacterial chemoreceptors: high- performance signaling in networked arrays*, Trends Biochem. Sci. 33 (2008), pp. 9–19.
[13] V. Sourjik, *Receptor clustering and signal processing in E. coli chemotaxis*, Trends Microbiol. 12 (2004), pp. 569–576.
[14] H.C. Berg, *The rotary motor of bacterial flagellar*, Annu. Rev. Biochem. 72 (2003), pp. 19–54.
[15] S.W. Reid, M.C. Leake, J.H. Chandler, C.L.J.P. Armitage, and R.M. Berry, *The maximum number of torque-generating units in the flagellar motor of Escherichia coli is at least 11*, 103 (2006), pp. 8066–8071.
[16] M.C. Leake, J.H. Chandler, G.H. Wadhams, F. Bai, R.M. Berry, and J.P. Armitage, *Stoichiometry and turnover in single, functioning membrane protein complexes*, Nature 443 (2006), pp. 355–358.

[17] R.M. Macnab, *How bacteria assemble flagella*, Annu. Rev. Microbiol. 57 (2003), pp. 77–100.
[18] E.M. Purcell, *Life at low Reynolds number*, Am. J. Phys. 45 (1977), pp. 3–11.
[19] E.M. Sevick, R. Prabhakar, S.R. Williams, and D.J. Searles, *Fluctuation theorems*, Annu. Rev. Phys. Chem. 59 (2008), pp. 603–633.
[20] H. Eyring, *The activated complex and the absolute rate of chemical reactions*, Chem. Rev. 17 (1935), pp. 65–77.
[21] H.A. Kramers, *Brownian motion in a field of force and the diffusion model of chemical reactions*, Physica 7 (1940), pp. 284–304.
[22] A.F. Huxley, *Muscle structure and theories of contraction*, Prog. Biophys. Biophys. Chem. 7 (1957), pp. 255–318.
[23] A.F. Huxley and R.M. Simmons, *Proposed mechanism of force generation in striated muscle*, Nature 233 (1971), pp. 533–538.
[24] H. Noji, R. Yasuda, M. Yoshida, and K. Kinosita, *Direct observation of the rotation of F_1-ATPase*, Nature 386 (1997), pp. 299–302.
[25] J.P. Abrahams, A.G.W. Leslie, R. Lutter, and J.E. Walker, *Structure at 2.8 A resolution of F_1-ATPase from bovine heart mitochondria*, Nature 370 (1994), pp. 621–628.
[26] C. Bustamante, D. Keller, and G. Oster, *The physics of molecular motors*, Acc. Chem. Res. 34 (2001), pp. 412–420.
[27] J. Xing, F. Bai, R. Berry, and G. Oster, *Torque–speed relationship of the bacterial flagellar motor*, Proc. Natl. Acad. Sci. USA 103 (2006), pp. 1260–1265.
[28] M. Silverman and M. Simon, *Flagellar rotation and the mechanism of bacterial motility*, Nature 249 (1974), pp. 73–74.
[29] A. Ashkin, J.M. Dziedzic, J.E. Bjorkholm, and S. Chu, *Observation of a single-beam gradient force optical trap for dielectric particles*, Opt. Lett. 11 (1986), p. 288.
[30] F. Gittes and C.F. Schmidt, *Interference model for back-focal-plane displacement detection in optical tweezers*, Opt. Lett. 23 (1998), pp. 7–9.
[31] H. Wang and G. Oster, *The Stokes efficiency for molecular motors and its applications*, Europhys. Lett. 57 (2002), p. 140.
[32] Y. Sowa, A.D. Rowe, M.C. Leake, T. Yakushi, M. Homma, A. Ishijima, and R.M. Berry, *Direct observation of steps in rotation of the bacterial flagellar motor*, Nature 437 (2005), pp. 916–919.
[33] R. Yasuda, H. Noji, M. Yoshida, K. Kinosita, and H. Itoh, *Resolution of distinct rotational substeps by submillisecond kinetic analysis of F_1-ATPase*, Nature 410 (2001), pp. 898–904.
[34] W.S. Ryu, R.M. Berry, and H.C. Berg, *Torque-generating units of the flagellar motor of Escherichia coli have a high duty ratio*, Nature 403 (2000), pp. 444–447.
[35] T. Yorimitsu and M. Homma, *Na^+-driven flagellar motor of Vibrio*, Biochim. Biophys. Acta (BBA) – Bioenergetics 1505 (2001), pp. 82–93.
[36] Y. Asai, T. Yakushi, I. Kawagishi, and M. Homma, *Ion-coupling determinants of Na^+-driven and H^+-driven flagellar motors*, J. Molec. Biol. 327 (2003), pp. 453–463.
[37] C. Lo, M.C. Leake, T. Pilizota, and R.M. Berry, *Nonequivalence of membrane voltage and ion-gradient as driving forces for the bacterial flagellar motor at low load*, Biophys. J. 93 (2007), pp. 294–302.
[38] X. Chen and H.C. Berg, *Torque–speed relationship of the flagellar rotary motor of Escherichia coli*, Biophys. J. 78 (2000), pp. 1036–1041.
[39] Y. Inoue, C. Lo, H. Fukuoka, H. Takahashi, Y. Sowa, T. Pilizota, G.H. Wadhams, M. Homma, R.M. Berry, and A. Ishijima, *Torque–Speed relationships of Na^+-driven chimeric flagellar motors in Escherichia coli*, J. Molec. Biol. 376 (2008), pp. 1251–1259.
[40] H.C. Berg and L. Turner, *Torque generated by the flagellar motor of Escherichia coli*, Biophys. J. 65 (1993), pp. 2201–2216.
[41] R.M. Berry and H.C. Berg, *Torque generated by the flagellar motor of Escherichia coli while driven backward*, Biophys. J. 76 (1999), pp. 580–587.
[42] X. Chen and H.C. Berg, *Solvent-isotope and pH effects on flagellar rotation in Escherichia coli*, Biophys. J. 78 (2000), pp. 2280–2284.
[43] C.V. Gabel and H.C. Berg, *The speed of the flagellar rotary motor of Escherichia coli varies linearly with protonmotive force*, Proc. Natl. Acad. Sci. USA 100 (2003), pp. 8748–8751.
[44] R.M. Berry and H.C. Berg, *Torque generated by the flagellar motor of Escherichia coli while driven backward*, Biophys. J. 76 (1999), pp. 580–587.
[45] F. Bai, C. Lo, R.M. Berry, and J. Xing, *Model studies of the dynamics of bacterial flagellar motors*, Biophys. J. 96 (2009), pp. 3154–3167.
[46] J. Yuan and H.C. Berg, *Resurrection of the flagellar rotary motor near zero load*, Proc. Natl. Acad. Sci. 105 (2008), pp. 1182–1185.
[47] K. Svoboda, C.F. Schmidt, B.J. Schnapp, and S.M. Block, *Direct observation of kinesin stepping by optical trapping interferometry*, Nature 365 (1993), pp. 721–727.
[48] M.J. Schnitzer, K. Visscher, and S.M. Block, *Force production by single kinesin motors*, Nat. Cell Biol. 2 (2000), pp. 718–723.
[49] T. Pilizota, Y. Sowa, and R.M. Berry, Single molecule studies of rotary molecular motors, in *Handbook of Single-Molecule Biophysics*, A.M. van Oijen and P. Hinterdorfer, eds., Springer, Berlin, 2009.
[50] D.R. Thomas, N.R. Francis, C. Xu, and D.J. DeRosier, *The three-dimensional structure of the flagellar rotor from a clockwise-locked mutant of Salmonella enterica Serovar typhimurium*, J. Bacteriol. 188 (2006), pp. 7039–7048.
[51] A.D. Samuel and H.C. Berg, *Fluctuation analysis of rotational speeds of the bacterial flagellar motor*, Proc. Natl. Acad. Sci. USA 92 (1995), pp. 3502–3506.
[52] A.D. Samuel and H.C. Berg, *Torque-generating units of the bacterial flagellar motor step independently*, Biophys J. 71 (1996), pp. 918–923.
[53] S.M. Block, D.F. Blair, and H.C. Berg, *Compliance of bacterial flagella measured with optical tweezers*, Nature 338 (1989), pp. 514–518.